inorganics

MDPI

Article

Exploring the Interdependence between Electronically Unfavorable Situations and Pressure in a Chalcogenide Superconductor

Kai S. Fries and Simon Steinberg *

Institute of Inorganic Chemistry, RWTH Aachen University, Landoltweg 1, D-52074 Aachen, Germany
* Correspondence: simon.steinberg@ac.rwth-aachen.de

Abstract: The development of solids with the requested chemical and physical properties requires a thorough understanding of their electronic structures, as proper knowledge of the electronic structure of a given solid provides invaluable information regarding its properties. In this context, recent research on two competing sorts of electronic instabilities in chalcogenide superconductors stimulated us to explore the interdependence between these instabilities and another aspect, pressure, which was previously shown to influence the presence of a superconducting state in diverse solids. To accomplish our goal, we carried out pressure-dependent examinations of the electronic structures of two tellurides, YTe and $YTe_{0.97}$, which were inspected as prototypes in our explorations based on quantum-chemical means. In addition to our pressure-dependent explorations of the electronic structures, we also performed chemical bonding analyses to reveal the subtle interplay between pressure and two sorts of electronically unfavorable situations.

Keywords: electronic structures; tellurides; superconductors

Citation: Fries, K.S.; Steinberg, S. Exploring the Interdependence between Electronically Unfavorable Situations and Pressure in a Chalcogenide Superconductor. *Inorganics* **2023**, *11*, 61. https://doi.org/10.3390/inorganics11020061

Academic Editors: Rubicelia Vargas and Jorge Garza

Received: 29 December 2022
Revised: 21 January 2023
Accepted: 24 January 2023
Published: 27 January 2023

1. Introduction

In the quest for technologies capable of solving future challenges, there is a critical need to develop solid-state materials that can serve as components in such technologies [1]. In this regard, chalcogenides are of particular interest among chemists, physicists, and engineers, as several representatives of this remarkable family of solids are located at the forefront of diverse fields of research [2]. These areas of research include explorative efforts concerning phase-change data storage devices [3,4], thermoelectrics [5,6], topological insulators [7], and superconductors [8,9], to name just a few. The design of solids considered for a particular task also requires a proper understanding of their electronic structures, as knowledge of the electronic structure of a given solid provides invaluable information regarding its chemical and physical properties [10].

In the case of tellurides, the relationships between the crystal and electronic structures have typically been [11,12] interpreted using the Zintl–Klemm–Busmann concept, which was originally developed for intermetallics, which exclusively consist of main-group elements [13–18]. In the framework of this approach, the valence electrons are considered to be transferred from the more electropositive to the more electronegative elements, which form clusters and frameworks that are isostructural to the structural fragments of the elements, which are isoelectronic to the aforementioned anions. Indeed, this approach works well in recognizing the interdependence between the structural and electronic features of tellurides solely containing alkali and alkaline-earth metals [19]; however, the applicability of this approach to tellurides containing *p*- or *d*-block elements faces some hurdles. For instance, recent research on tellurides comprising *p*-block elements revealed a remarkable electronic state dubbed metavalency [20–23]. In this state, the valence electrons are expected to be delocalized across multiple centers, while a metallic state is not achieved [24,25].

While the aforementioned explorations focused on the nature of the electronic structures in tellurides only containing *s*- and *p*-block elements, additional research concentrated on the electronic structures of tellurides comprising early and/or late transition metals [24,26–36]. The outcomes of such research showed that the factors controlling the formation of a given structure model are rather subtle, meaning that applications of the Zintl–Klemm–Busmann concept hardly help to recognize the relationships between the crystal and electronic structures. In this regard, recent research [37] on a series of chalcogenide superconductors also demonstrated that two competing types of electronically unfavorable situations influence the presence or absence of defects in the crystal structures of these materials.

In fact, controlling these types of instabilities is highly relevant, as the occurrence of defects in the crystal structure of a given solid also affects its electronic structure and, ultimately, its properties. In the case of chalcogenide superconductors, such defects in the crystal structure were shown [38,39] to influence the transitions from the metallic to superconducting states, as the occurrence of a superconducting state is also strongly related to the nature of the electronic structure of a given material [40–42]. In this context, there is also a need to explore the impacts of further aspects influencing the presence of a superconducting state with regard to the aforementioned competition. Another aspect that has been found to influence the accomplishment of a superconducting state is the application of external pressure to a superconducting material [43]. In light of this, our impetus was stimulated to explore the role of pressure in the competition between the two different types of electronic instabilities using the example of a chalcogenide superconductor, i.e., YTe. In the following contribution, we present the results of our explorations based on quantum-chemical means.

2. Results and Discussion

To explore the interdependence between the two types of electronic instabilities and pressure with regard to the materials' properties, we selected the rock-salt-type chalcogenide superconductor [38] YTe as the prototype for our explorations. This telluride was selected because recent research on YTe [9,24] suggested that the two sorts of competing electronically favorable situations that will be inspected in the present explorations could also be present in this binary telluride. While the examinations of the electronic band structures will reveal if flat bands cross the Fermi levels and lead to one sort of electronic instability [43,44], the chemical bonding analyses will show the feasible presence of occupied antibonding states, which are expected to be the other type of electronically unfavorable situation [37]. As the competition between these two sorts of electronic instabilities is expected to be related to the presence or absence of defects in the crystal structure, a structure model containing vacancies, i.e., $Y_{32}Te_{31}$, was also constructed following the approach employed in the aforementioned research (Figure 1) [9,37]. Furthermore, the inspected pressure range was chosen after consideration of a previously reported pressure-dependent phase transition of this telluride. More specifically, prior explorations [45] concerning the binary YTe revealed a pressure-dependent phase transition from the NaCl-type to the CsCl-type of structure at 14 GPa. Moreover, structural optimizations and pressure-dependent computations of the total energies were performed for both tellurides prior to the examinations of the electronic band structures and chemical bonding analyses (see Materials and Methods). In this regard, it should be noted that the lattice parameters of the optimized YTe structure model (Figure 1) are quite close to the parameters (a = 6.114 Å) that were experimentally [46] determined for that telluride at p = 1 atm. An additional comparison of the computed total energies of the YTe and $Y_{32}Te_{31}$ (Table 1) reveals that the total energies of both tellurides increase as the pressure increases. Furthermore, increasing the pressure also leads to reductions in the lattice parameters, and considering the cubic lattice settings of both tellurides, the unit cell volumes (Figure 1). These trends follow a tendency typically [47] expected for the total energy and unit cell volume as functions of the pressure, meaning that we can proceed with the analyses of the electronic band structures.

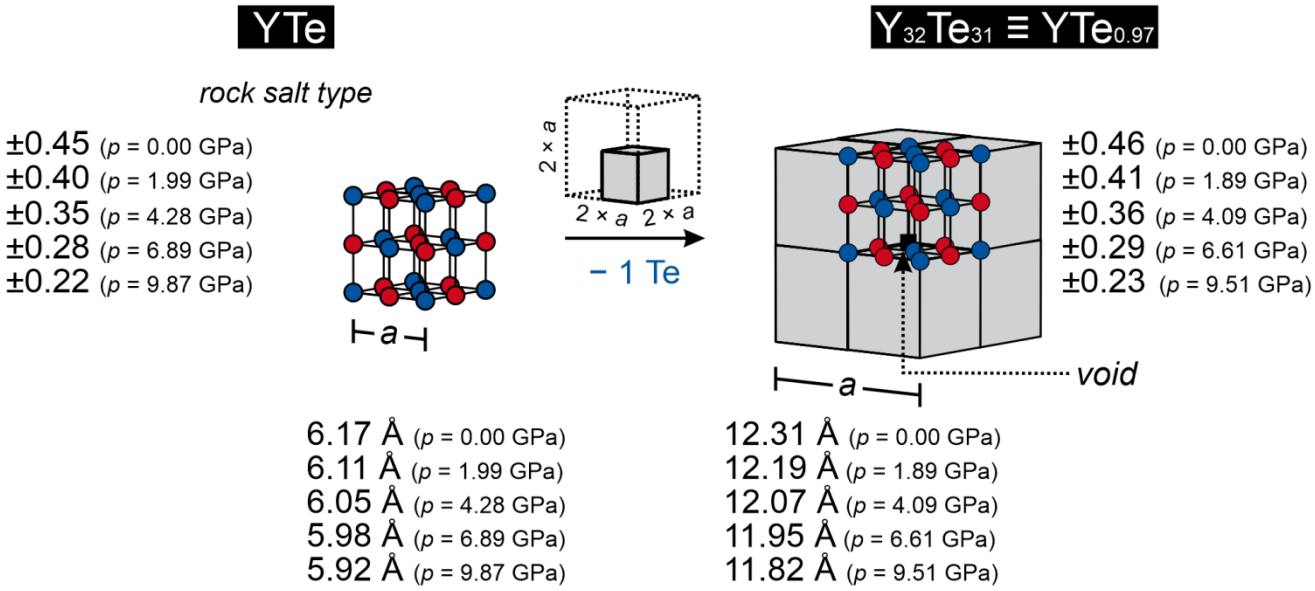

Figure 1. Representations of the crystal structures of YTe and $Y_{32}Te_{31}$: the structure model of the latter telluride was constructed based on the crystal structure of YTe, an approach that has also been utilized in previous studies (see main text). Furthermore, the respective averaged Mulliken charges have been included (in units of the elementary charge *e*).

Table 1. Pressure ranges (*p*), total energies (E_{tot}) per formula units (f.u.), and percentage contributions of the different bonding interactions to the net bonding capacities in YTe and $Y_{32}Te_{31}$. The percentages of the different bonding interactions were calculated using the approach described below.

YTe				$Y_{32}Te_{31} \equiv YTe_{0.97}$			
***p* [GPa]**	**E_{tot} [eV/f.u.]**	**% (Y–Te)**	**% (Y–Y)**	***p* [GPa]**	**E_{tot} [eV/f.u.]**	**% (Y–Te)**	**% (Y–Y)**
0.00	−12.290	89.40	10.60	0.00	−12.013	88.09	11.91
1.99	−12.198	89.27	10.73	1.89	−12.003	88.00	12.00
4.28	−12.165	89.15	10.85	4.09	−11.972	87.91	12.09
6.89	−12.107	89.05	10.95	6.61	−11.917	87.81	12.19
9.87	−12.022	88.94	11.06	9.51	−11.835	87.71	12.29

To gain an initial insight into the interdependence between the two competing sorts of electronic instabilities and the pressure, we followed up with an inspection of the electronic band structures (Figures 2 and 3) and the respective density-of-states (DOS) curves (Figures 4 and 5). An examination of the DOS curves for the YTe and $Y_{32}Te_{31}$ indicates that the states close to the Fermi levels, E_F, originate to a large extent from the Y-4*d* and Te-5*p* atomic orbitals. As the states located close to the Fermi level of a given solid usually largely contribute to its bonding, it can be concluded that the bonds in the YTe and $Y_{32}Te_{31}$ originate from the aforementioned atomic orbitals to a large extent. An additional inspection of the electronic band structures shows that the dispersions of the bands are enlarged as the pressure is increased. This outcome is in good agreement with the trend that is usually [47,48] expected for the dispersion of a given band with regard to pressure. While these pressure-induced changes in the electronic structure do not provoke any substantial alterations in the electronic band structure of the YTe, remarkable changes are evident in the electronic band structure of the $Y_{32}Te_{31}$ as the pressure is increased. In particular, a flat band that crosses the E_F at the **M**-point at 0.00 GPa is moved to a position close to the Fermi level as the pressure is increased. This change in the electronic band structures also translates into a modification of the Fermi level characteristics of the $Y_{32}Te_{31}$. At 0.00 GPa, the E_F in the $Y_{32}Te_{31}$ is located at a maximum of the DOS, whereas the Fermi

levels are located at the minima of the DOS for $p > 0.00$ GPa. In connection with the changes in the Fermi level characteristics in the $Y_{32}Te_{31}$, it is remarkable that the Fermi levels are positioned at the minima of the DOS for $p > 0.00$ GPa, as such a situation is often [49–52] considered to suggest an electronically favorable situation; however, a comparison of the pressure-dependent total energies of the $Y_{32}Te_{31}$ (Table 1) clearly demonstrates that the structure model at 0.00 GPa corresponds to the lowest total energy and, hence, is the most preferred structure model to be formed among all the inspected $Y_{32}Te_{31}$ models. As no flat band crosses the Fermi level of the YTe for $p \geq 0$ GPa, the examination of the electronic band structures suggests that there is also a certain tendency to form YTe rather than the tellurium-deficient $Y_{32}Te_{31}$.

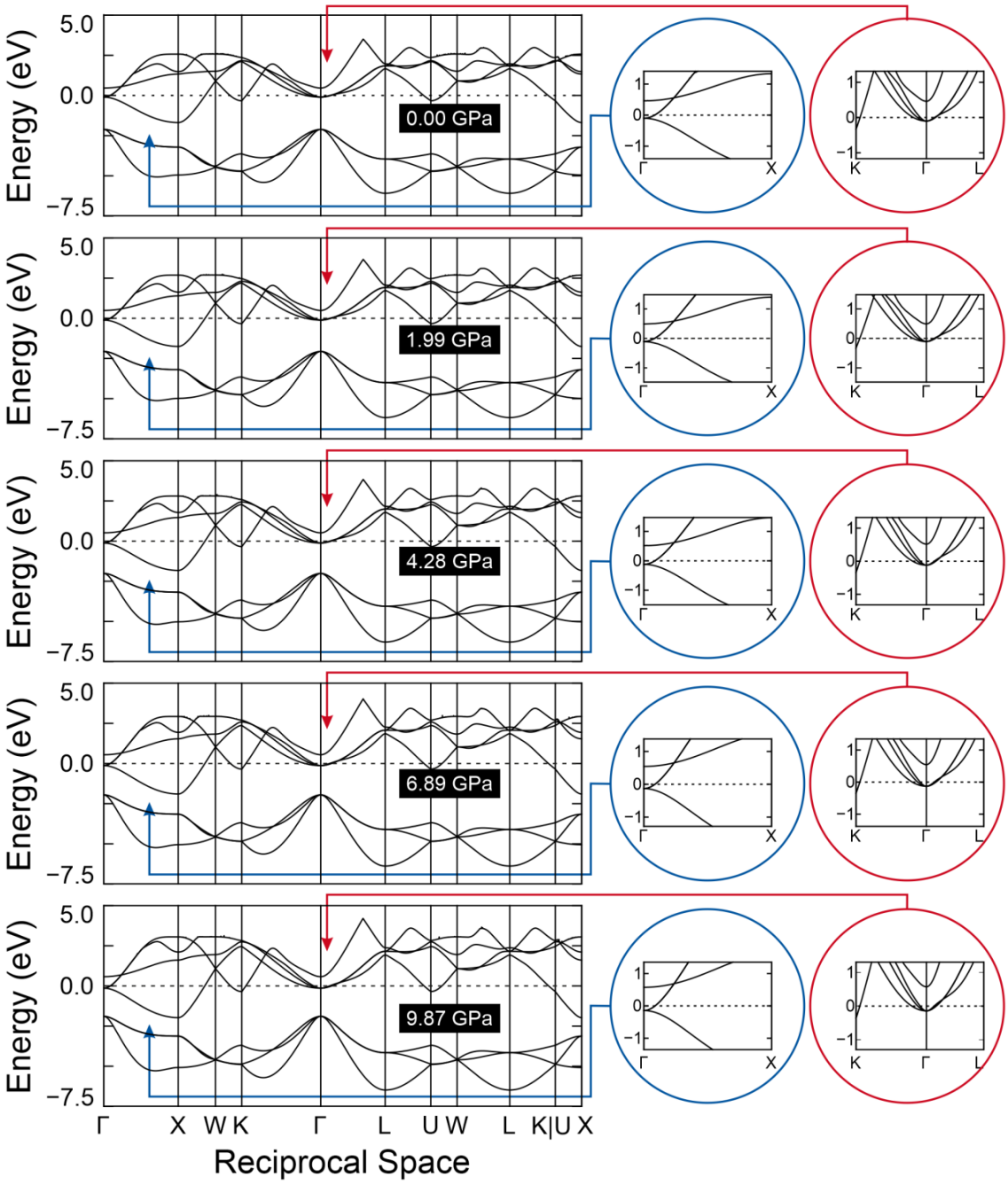

Figure 2. Pressure-dependent electronic band structures of the rock-salt-type YTe: energy regions that comprise flat bands positioned close to the Fermi levels, E_F, are shown in the insets, while the dotted horizontal lines represent the Fermi levels.

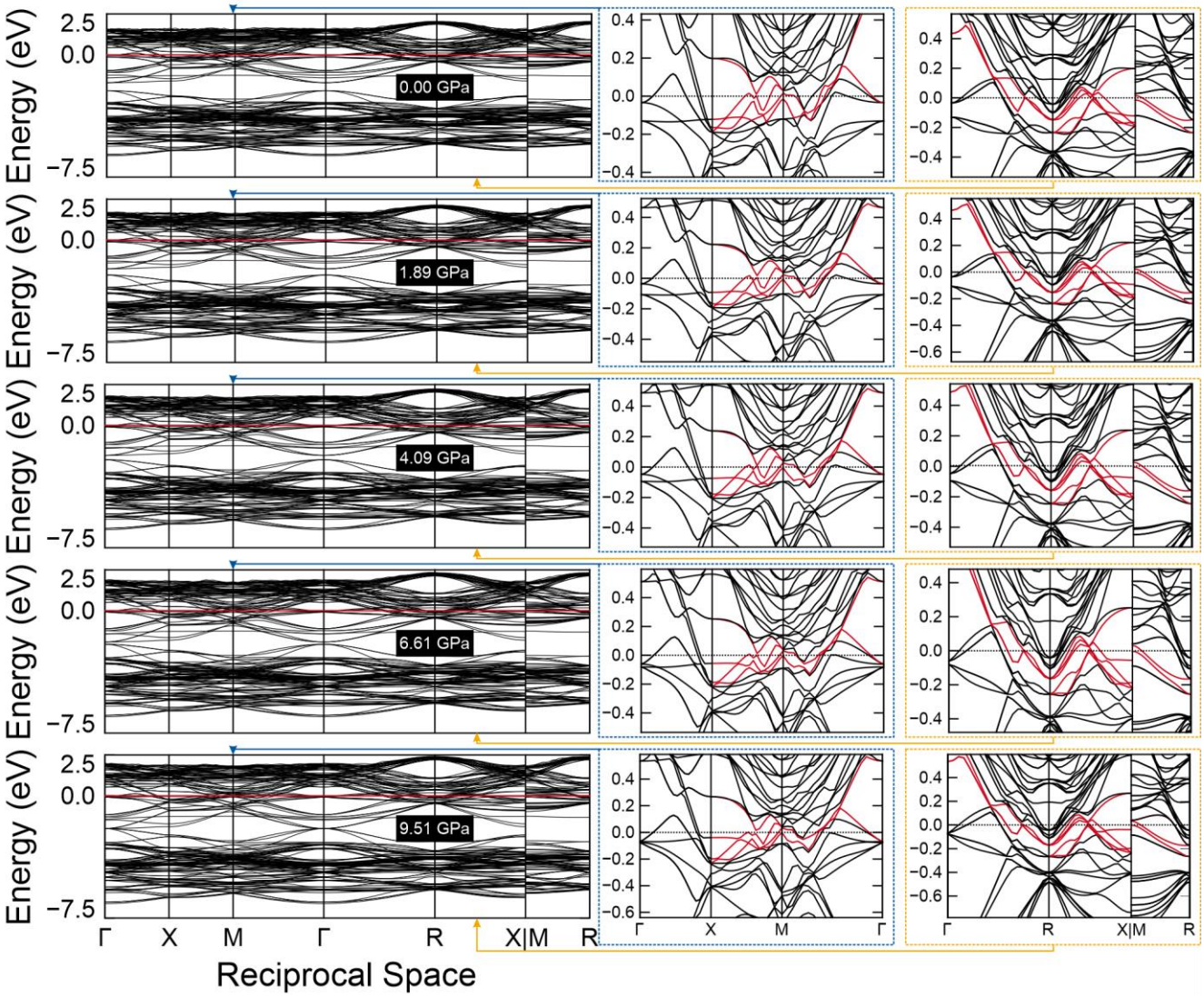

Figure 3. Pressure-dependent electronic band structures of the tellurium-deficient $Y_{32}Te_{31}$: energy regions that contain flat bands located close to the Fermi levels, E_F, are shown in the insets. The Fermi levels are indicated by the red horizontal lines in the diagrams showing the electronic band structures in the wider energy ranges, and by the dotted horizontal lines in the corresponding insets. Bands exhibiting maxima, minima, and saddle points at the Fermi levels are highlighted in red in the insets. Note that the dispersion of the bands increases (e.g., at the Γ-point), as the pressure increases.

In summary, the examinations of the electronic band structures and DOS curves of the YTe revealed that there are no substantial changes in the features at the E_F as the pressure is increased. On the other hand, increasing the pressure influences the Fermi level characteristics of the $Y_{32}Te_{31}$. Accordingly, the aforementioned explorations provided an insight into the interplay between the pressure and one sort of electronically unfavorable situation, i.e., the presence of flat bands at the E_F; however, these examinations did not provide any information about the relationship between the pressure and the other sort of electronically unfavorable situation that was mentioned in the Introduction (see above). As the other sort of electronically unfavorable situation was related to the bonding situations in the inspected chalcogenide superconductors, we followed up with a chemical bonding analysis based on the Mulliken charges (Figure 1), projected crystal orbital Hamilton populations (–pCOHPs; Figures 4 and 5), and the electron localization functions (ELFs; Figure 6) of YTe and $Y_{32}Te_{31}$.

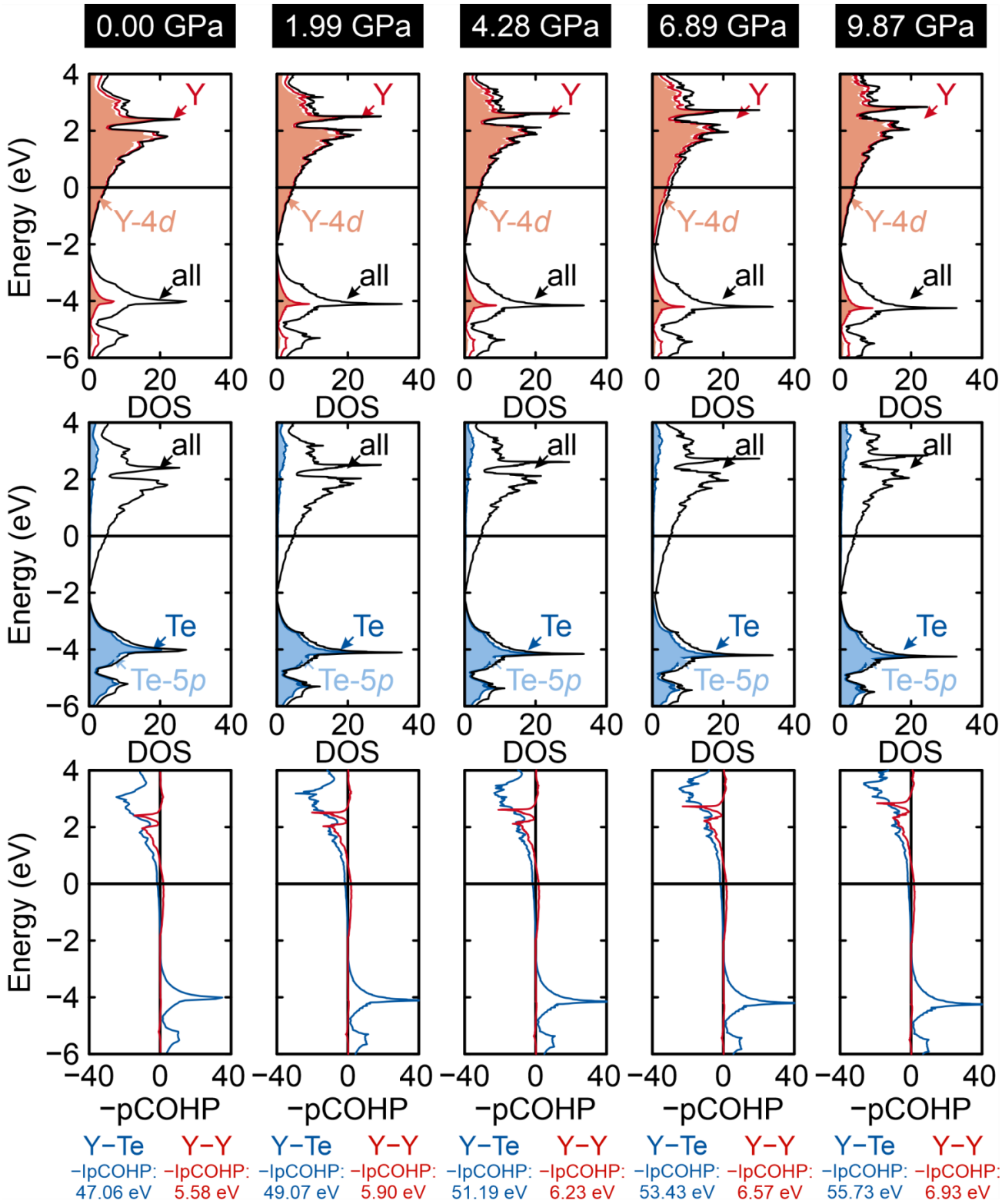

Figure 4. Pressure-dependent density-of-states (DOS) curves and projected crystal orbital Hamilton populations (–pCOHP) of the rock-salt-type YTe. The Fermi levels, E_F, are indicated by the black horizontal lines, while the cumulative –IpCOHP/cell values (see main text) are shown below the corresponding –pCOHP diagrams. Please note that the respective labels were located at the same relative positions within all the DOS diagrams so that the pressure-induced changes in the DOS curves could be recognized by inspecting the environments of the corresponding labels.

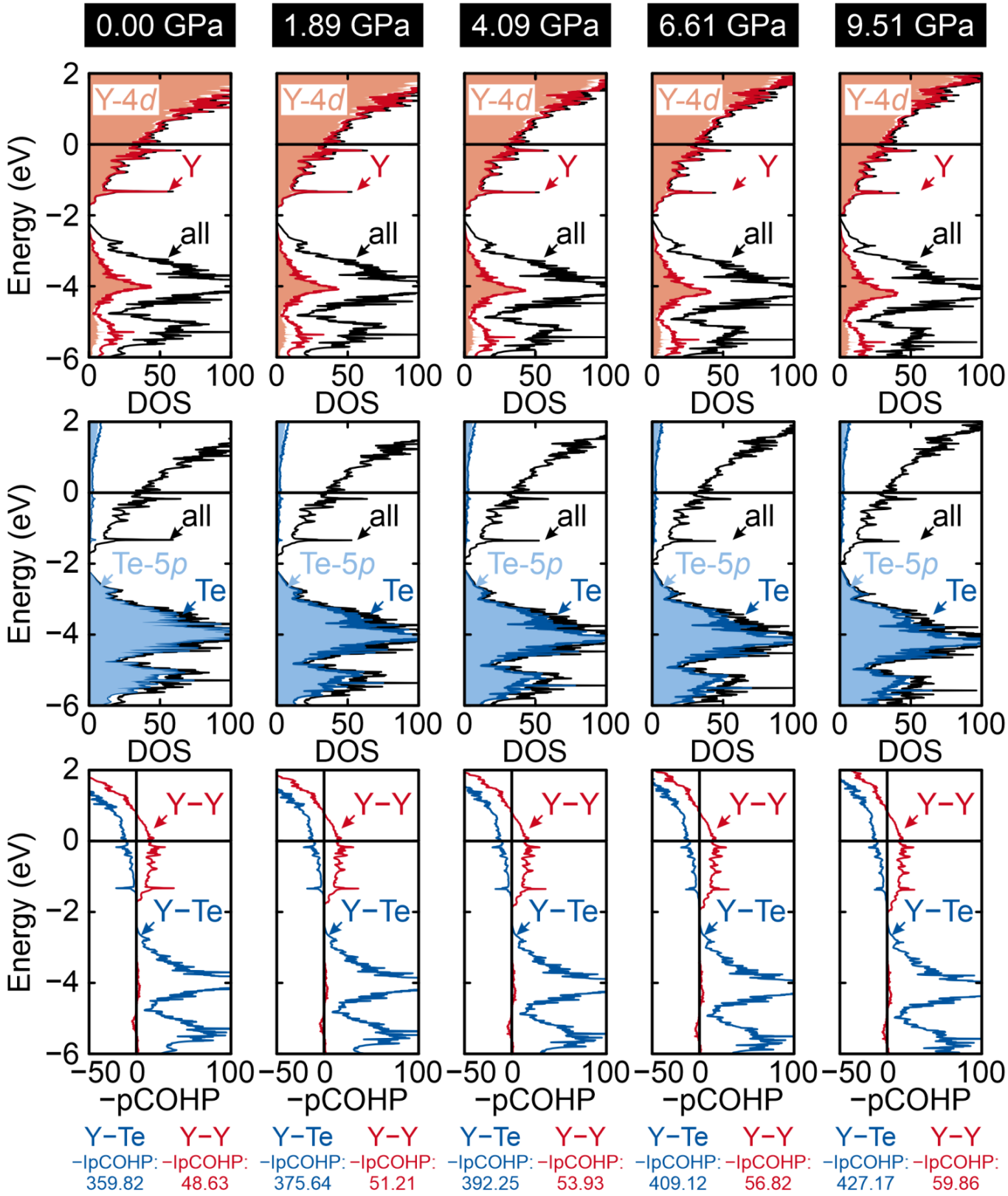

Figure 5. Pressure-dependent density-of-states (DOS) curves and projected crystal orbital Hamilton populations (–pCOHP) of the tellurium-deficient $Y_{32}Te_{31}$. The Fermi levels, E_F, are denoted by the black horizontal lines, while the cumulative –IpCOHP/cell values (see main text) are included below the respective –pCOHP diagrams.

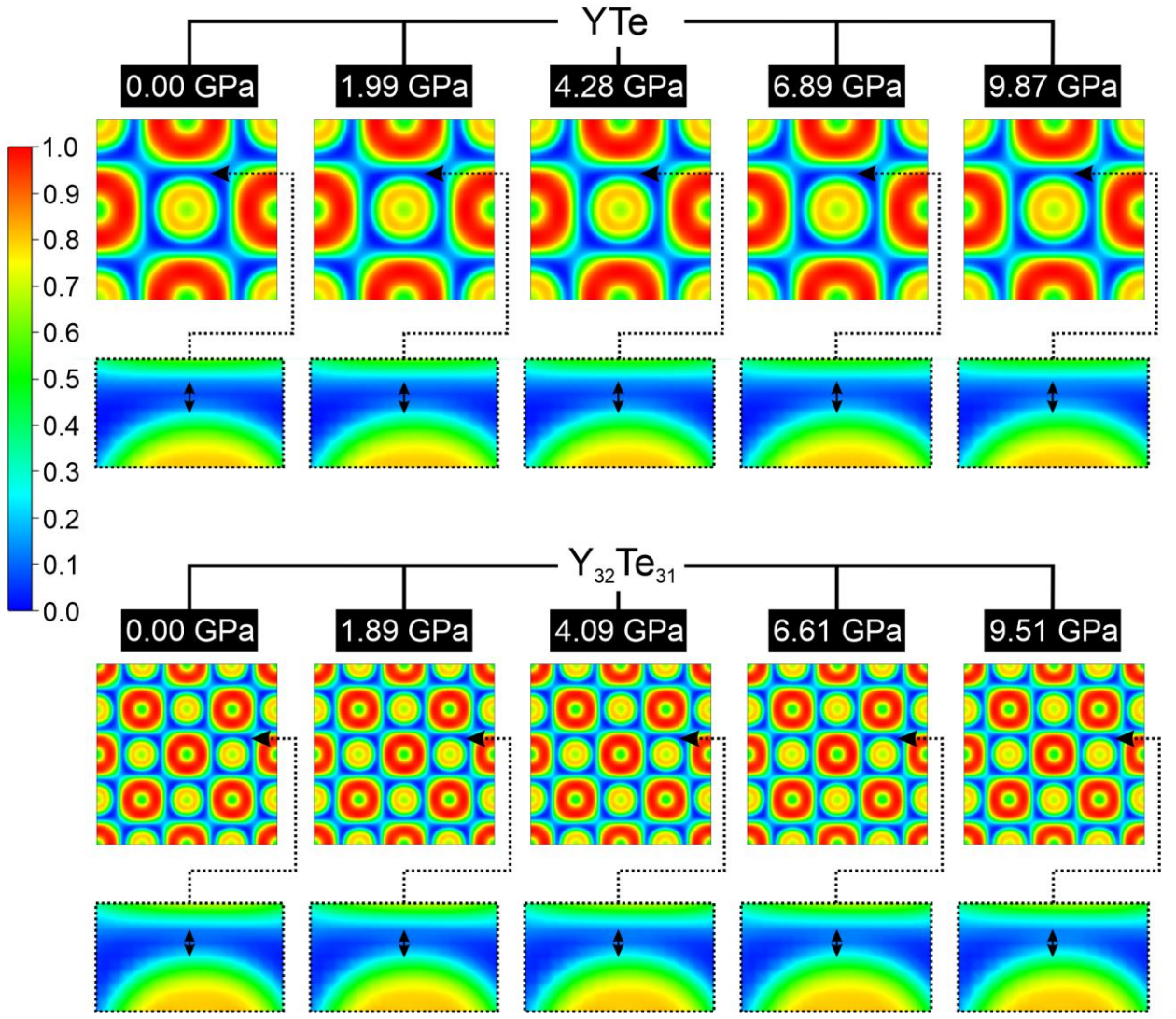

Figure 6. Representations of the electronic localization functions (ELFs) of the YTe (**top**) and the tellurium-deficient $Y_{32}Te_{31}$ (**bottom**) with regard to the pressure. Magnified representations of sections of the respective ELFs are shown in the insets: the arrows have been included in order to highlight extremely small changes in the distances between certain domains.

An inspection of the Mulliken charges of the YTe and $Y_{32}Te_{31}$ (Figure 1) indicates that the computed charges evidently differ from the charges that, for instance, are expected based on a Zintl–Klemm treatment suggesting a full valence electron transfer, i.e., YTe $\equiv (Y^{3+})(Te^{2-})(e^{-})$. Accordingly, the Y–Te interactions cannot be described as ionic, as ionic bonds are supposed [53] to be located between closed-shell species carrying opposite electronic charges. In order to identify the nature of the bonding in the YTe and $Y_{32}Te_{31}$, we examined the projected crystal orbital Hamilton populations and the respective integrated values (–IpCOHP; Figures 4 and 5). In this regard, it should be noted that a direct comparison between the –IpCOHP values determined for the compounds with dissimilar compositions cannot be made, as the electrostatic potential of each density-functional-theory-based computation is set to an arbitrary "zero" energy, whose relative position may vary from system to system [47]. Therefore, we used a well-established approach [54,55] to overcome this issue and, ultimately, reveal similarities as well as differences in the bonding situations of the YTe and $Y_{32}Te_{31}$. Within the framework of this method, the cumulative –IpCOHP/cell values (Figures 4 and 5), i.e., the sums of all the –IpCOHP/bond values

for the respective sorts of interatomic contacts within one unit cell, were projected as percentages of the net bonding capabilities (Table 1).

An examination of the –pCOHP diagrams for the YTe and $Y_{32}Te_{31}$ reveals that the heteroatomic Y–Te interactions change from the bonding to antibonding states below the Fermi levels, E_F (Figures 4 and 5). Although the antibonding Y–Te states are occupied below the E_F, the cumulative –IpCOHP/cell values clearly point to a net bonding character for these heteroatomic interactions. Furthermore, the antibonding heteroatomic Y–Te states are counterbalanced by the bonding homoatomic Y–Y states, which show less bonding character relative to the heteroatomic Y–Te interactions. The Y–Y bonds are constructed based on the Y-4*d* atomic orbitals so that the crystal structures of the tellurides can also be viewed as yttrium networks that are oxidized by the tellurium atoms. This outcome is also in good agreement with previous research [56,57] showing analogies between the electronic structures of compounds containing transition-metal clusters and those of rock-salt-type transition-metal chalcogenides. As the electrons are rather delocalized within the Y–Y bonds, it is clear that the homoatomic interactions exhibit less bonding character. As the heteroatomic Y–Te interactions show more bonding character than the Y–Y interactions, it can be inferred that the electrons must be localized within the Y–Te contacts. Under consideration of the valence electron transfers from the yttrium to the tellurium atoms (Figure 1), the Y–Te bonds should be depicted as polar covalent.

As the Y–Te interactions show more bonding character and, accordingly, higher cumulative –IpCOHP/cell values than the Y–Y interactions, the former contacts also correspond to higher percentages of net bonding capacities than the latter bonds (Table 1). A comparison between the percentage contributions of the diverse interactions and the net bonding capacities also indicates that the percentage contributions of the Y–Te contacts are higher in the YTe than in the tellurium-deficient $Y_{32}Te_{31}$, while, in turn, the Y–Y bonds make higher percentage contributions to the bonding capacities in the $Y_{32}Te_{31}$ than in the YTe. This difference in the bonding situations is caused by the reduction in the numbers of Y–Te contacts per formula units from the YTe to the $Y_{32}Te_{31}$ ($\equiv YTe_{0.97}$). As a consequence, the amounts of antibonding states are also reduced from the YTe to the $Y_{32}Te_{31}$ ($\equiv YTe_{0.97}$), while Y–Y bonding is a more evident factor in the $Y_{32}Te_{31}$ than in the YTe. As the overall bonding is optimized for the tellurium-deficient $Y_{32}Te_{31}$, the outcome of the chemical bonding analysis clearly implies that there is a tendency to form $Y_{32}Te_{31}$ rather than YTe.

Accordingly, the results of the bonding analysis and the examinations of the electronic band structures evidently show that there is a competition between the two sorts of electronically favorable situations, which are related to the presence or absence of vacancies in the crystal structure of the tellurides. In the tellurium-deficient $Y_{32}Te_{31}$ ($\equiv YTe_{0.97}$), the chemical bonding is optimized, meaning that this model should be preferred based on the bonding analyses. On the other hand, the inspections of the Fermi level characteristics, especially the search for (electronically unfavorable) flat bands at the Fermi levels, suggest that YTe should be preferred rather than $Y_{32}Te_{31}$. Yet, how does the increase in the pressure affect the nature of the chemical bonding in YTe and $Y_{32}Te_{31}$ and, hence, this sort of electronically unfavorable situation?

An inspection of the pressure-dependent –pCOHP diagrams for both the YTe and the tellurium-deficient $Y_{32}Te_{31}$ (Figures 4 and 5) shows that increasing the pressure results in certain magnifications of the cumulative Y–Te and Y–Y –IpCOHP/cell values. This outcome can be explained based on the decrease in the distances between the yttrium and tellurium atoms due to the enlargement of the pressure: as the pressure increases, the interatomic distances decrease so that there is a more effective overlap of the atomic orbitals involved in the diverse bonds. Finally, this more effective overlap of the atomic orbitals translates into an enlargement of the diverse –IpCOHP values, as determined based on the pressure-dependent –pCOHP diagrams. In addition to this aspect, there is also another point that can account for the pressure-dependent trend of the –IpCOHP values: increasing the pressure also leads to a decrease in the Mulliken charges (Figure 1), meaning that there is less valence electron transfer within the Y–Te separations, whose nature becomes more

covalent as the pressure increases, while the yttrium network is less oxidized. Notably, the increase in the –IpCOHP values is slightly more pronounced for the homoatomic Y–Y contacts than for the heteroatomic Y–Te interactions because the percentage contributions of the Y–Y interactions increase (Table 1) as the pressure is enlarged. In summary, one could guess that increasing the pressure results in minor optimizations of the overall bonding for both tellurides; however, the pressure-dependent total energies (Table 1) clearly indicate that the structure models existing at p = 0 GPa are the most preferred among the inspected models. This outcome can also be explained based on the decrease in the interatomic distances due to the enlargement of the external pressure: as the pressure is augmented, the distances between the cores of the atoms also decrease, meaning that the repulsion between the atoms is magnified. Yet, an inspection of the electron localization functions (ELFs) of the YTe and the tellurium-deficient $Y_{32}Te_{31}$ reveals that the changes in the electronic distributions in the domains within the inspected pressure ranges are rather hard to identify (Figure 6). An additional examination of the ELFs reveals that the domains are evident for the Y–Te separations, as a value of 0.12 is reached for the localization parameter η. Given recent research on the ELFs of solids containing rare-earth–chalcogenide contacts [35,58], this result also points to a certain polar-covalent character for the Y–Te bonds.

3. Materials and Methods

All the electronic structure computations were accomplished by means of the projector augmented wave (PAW) method [59], as implemented in the Vienna Ab initio Simulation Package (VASP) [60–64] by Kresse and Joubert. Prior to the electronic band structure computations, structural optimizations, including the lattice parameters and atomic positions, were completed for both inspected tellurides using the aforementioned PAW technique. After the structural optimizations leading to the fully relaxed structure models had been completed, the structure models occurring at p > 0 GPa were constructed based on the models at 0 GPa. These steps were performed using a previously developed [65] routine that has already been largely [66] employed elsewhere. The correlation and exchange in all the computations were described by the generalized gradient approximation of Perdew, Burke, and Ernzerhof [67] (GGA–PBE), while the cutoff energy was set to 500 eV in all the computations. Sets of 16 × 16 × 16 and 8 × 8 × 8 **k**-points were employed to sample the first Brillouin zones in the YTe and "$Y_{32}Te_{31}$" for the reciprocal space integrations, while all the computations were expected to be converged as the energy differences between the two iterative steps fell at 10^{-8} eV and (10^{-6} eV) for the electronic (and ionic) relaxations. In the case of the electronic band structures, the paths in the reciprocal space were generated with the aid of the Automatic Flow (AFLOW) code [68], while the computed data were further processed using the Python Materials Genomics code (pymatgen) [69].

To explore the nature of the bonding in the two tellurides, the Mulliken charges, projected crystal orbital Hamilton populations (–pCOHPs) [55], and electron localization functions (ELFs) [70,71] were inspected. The ELFs were computed using the aforementioned PAW method and visualized with the aid of the Visualization for Electronic and Structural Analysis (VESTA) program [72]. In the case of the –pCOHPs, the entries of the density-of-states (DOS) matrices were weighted with the respective Hamilton matrix elements to reveal the bonding, nonbonding, and antibonding interactions in the two tellurides. As the crystal orbitals utilized in the constructions of the –pCOHPs required the use of local basis sets, whose nature is in stark contrast to the delocalized one of the plane-waves, the results of the plane-wave-based computations had to be transferred to Slater-type orbitals by means of transfer matrices. These projective transformations were accomplished by employing the Local Orbital Basis Suite Towards Electronic-Structure Reconstruction (LOBSTER) code [73–76], while the diverse –pCOHPs were visualized with the aid of the wxDragon code [77], which was also used to plot the electronic density-of-states (DOS) curves. In the framework of the aforementioned projective transformations [19], the gross populations were also computed and subtracted from the respective valence electron counts in order to obtain the Mulliken charges for every atom.

4. Conclusions

Understanding the electronic structures of materials is vital, as knowledge of the electronic structure of a given solid-state compound provides invaluable information regarding its chemical and physical properties. In the present contribution, we explored the interdependence between two sorts of electronic instabilities and pressure using the example of the rock-salt-type chalcogenide superconductor YTe. The outcome of our explorations based on quantum-chemical means indicates that the aforementioned competition between two electronically unfavorable situations, i.e., the presence of flat bands at the Fermi level and the optimization of the overall bonding, is indeed evident for this telluride. The competition between these two electronically unfavorable situations appears to influence the presence or absence of vacancies in the crystal structures when p = 0 GPa, while the impact of the pressure on the aforementioned competition is rather subtle.

While increasing the pressure does not provoke any significant changes in the electronic structure of the YTe, there are slight modifications, including the electronically unfavorable situation, in the band structure of the $Y_{32}Te_{31}$, for which the overall bonding is optimized regardless of the external pressure. Therefore, it might be assumed that increasing the pressure could support the formation of the tellurium-deficient $Y_{32}Te_{31}$; however, this effect appears to be rather small. At this point, one may also wonder why the pressure range inspected in this research was quite small when compared with the pressure ranges typically [78] explored in high-pressure experiments. Indeed, it was also intended to probe how increasing the pressure might alter the results of computations that are usually [79,80] accomplished based on fully relaxed structure models instead of the experimentally determined non-relaxed structure model. In the present case, the outcome of our explorations indicates that the role of pressure is rather subtle, thereby confirming our expectations within previous explorations in this particular field of research. Furthermore, the outcome of this study also indicates that a full picture of the electronic peculiarities of such telluride superconductors may be obtained from the fully relaxed structure models, which will be inspected in the framework of our ongoing research in the field of chalcogenides.

Author Contributions: Conceptualization, K.S.F. and S.S.; investigation, K.S.F. and S.S.; data curation, S.S.; writing—original draft preparation, S.S.; writing—review and editing, K.S.F. and S.S.; supervision, S.S.; funding acquisition, S.S. All authors have read and agreed to the published version of the manuscript.

Funding: This research was funded by the Deutsche Forschungsgemeinschaft (DFG; Bonn; project ID 511503255).

Data Availability Statement: The data presented in this study are available on request from the corresponding author.

Acknowledgments: The authors wish to thank Richard Dronskowski for the allocation of the computer cluster and research facilities at RWTH Aachen University. Furthermore, we wish to thank Peter Müller for the useful hints regarding the electron localization functions and Sebastian Hasenstab-Riedel for the fruitful discussion regarding the role of pressure in electronic structure computations.

Conflicts of Interest: The authors declare no conflict of interest.

References

1. Schmitt, D.C.; Drake, B.L.; McCandless, G.T.; Chan, J.Y. Targeted Crystal Growth of Rare Earth Intermetallics with Synergistic Magnetic and Electrical Properties: Structural Complexity to Simplicity. *Acc. Chem. Res.* **2015**, *48*, 612–618. [CrossRef]
2. Kanatzides, M.G. Discovery-Synthesis, Design, and Prediction of Chalcogenide Phases. *Inorg. Chem.* **2017**, *56*, 3158–3173. [CrossRef]
3. Wuttig, M.; Yamada, N. Phase-change materials for rewriteable data storage. *Nat. Mater.* **2007**, *6*, 824–832. [CrossRef] [PubMed]
4. Raoux, S.; Welnic, W.; Ielmini, D. Phase Change Materials and Their Application to Nonvolatile Memories. *Chem. Rev.* **2010**, *110*, 240–267. [CrossRef]
5. Snyder, G.J.; Toberer, E.S. Complex thermoelectric materials. *Nat. Mater.* **2008**, *7*, 105–114. [CrossRef]
6. Sootsman, J.R.; Chung, D.Y.; Kanatzidis, M.G. New and Old Concepts in Thermoelectric Materials. *Angew. Chem. Int. Ed.* **2009**, *48*, 8616–8639. [CrossRef] [PubMed]

7. Hazan, M.Z.; Kane, C.L. Colloquium: Topological Insulators. *Rev. Mod. Phys.* **2010**, *82*, 3045–3067. [CrossRef]
8. Nagata, S.; Atake, T. Survey of chalcogenide superconductors. *J. Therm. Anal. Calorim.* **1999**, *57*, 807–821. [CrossRef]
9. Fries, K.S.; Steinberg, S. Fermi-Level Characteristics of Potential Chalcogenide Superconductors. *Chem. Mater.* **2018**, *30*, 2251–2261. [CrossRef]
10. Miller, G.J. The "Coloring Problem" in Solids: How It Affects Structure, Composition and Properties. *Eur. J. Inorg. Chem.* **1998**, *1998*, 523–536. [CrossRef]
11. Böttcher, P. Tellurium-Rich Tellurides. *Angew. Chem. Int. Ed. Engl.* **1988**, *27*, 759–772. [CrossRef]
12. Papoian, G.A.; Hoffmann, R. Hypervalent Bonding in One, Two, and Three Dimensions: Extending the Zintl-Klemm Concept to Nonclassical Electron-Rich Networks. *Angew. Chem. Int. Ed.* **2000**, *39*, 2408–2448. [CrossRef]
13. Zintl, E. Intermetallische Phasen. *Angew. Chem.* **1939**, *52*, 1–6. [CrossRef]
14. Schäfer, H.; Eisenmann, B.; Müller, W. Zintl Phases: Transitions between Metallic and Ionic Bonding. *Angew. Chem. Int. Ed.* **1973**, *12*, 694–712. [CrossRef]
15. Janka, O.; Kauzlarich, S. Zintl Compounds. In *Encyclopedia of Inorganic and Bioinorganic Chemistry*; Scott, R.A., Ed.; WILEY-VCH: Weinheim, Germany, 2022.
16. Miller, G.J.; Schmidt, M.W.; Wang, F.; You, T.-S. Quantitative Advances in the Zintl-Klemm Formalism. *Struct. Bond.* **2011**, *139*, 1–55. [CrossRef]
17. Nesper, R. The Zintl-Klemm Concept—A Historical Survey. *Z. Anorg. Allg. Chem.* **2014**, *640*, 2639–2648. [CrossRef]
18. Gärtner, S.; Korber, N. Polyanions of Group 14 and Group 15 Elements in Alkali and Alkaline Earth Metal Solid State Compounds and Solvate Structures. *Struct. Bond.* **2011**, *140*, 25–57.
19. Ertural, C.; Steinberg, S.; Dronskowski, R. Development of a robust tool to extract Mulliken and Löwdin charges from plane waves and its applications to solid-state materials. *RSC Adv.* **2019**, *9*, 29821–29830. [CrossRef]
20. Wuttig, M.; Deringer, V.L.; Gonze, X.; Bichara, C.; Raty, J.-Y. Incipient Metals: Functional Materials with a Unique Bonding Mechanism. *Adv. Mater.* **2018**, *30*, 1803777. [CrossRef]
21. Raty, J.-Y.; Schumacher, M.; Golub, P.; Deringer, V.L.; Gatti, C.; Wuttig, M. A Quantum-Mechanical Map for Bonding and Properties in Solids. *Adv. Mater.* **2019**, *31*, 1806280. [CrossRef]
22. Cheng, Y.; Cojocaru-Mirédin, O.; Keutgen, J.; Yu, Y.; Küpers, M.; Schumacher, M.; Golub, P.; Raty, J.-Y.; Dronskowski, R.; Wuttig, M. Understanding the Structure and Properties of Sesqui-Chalcogenides (i.e., V_2VI_3 of Pn_2Ch_3 (Pn = Pnictogen, Ch = Chalcogen) Compounds) from a Bonding Perspective. *Adv. Mater.* **2019**, *31*, 1904316. [CrossRef]
23. Maier, S.; Steinberg, S.; Cheng, Y.; Schön, C.-F.; Schumacher, M.; Mazzarello, R.; Golub, P.; Nelson, R.; Cojocaru-Mirédin, O.; Raty, J.-Y.; et al. Discovering Electron-Transfer Driven Changes in Chemical Bonding in Lead Chalcogenides (PbX, where X = Te, Se, S, O). *Adv. Mater.* **2020**, *32*, 2005533. [CrossRef] [PubMed]
24. Simons, J.; Hempelmann, J.; Fries, K.S.; Müller, P.C.; Dronskowski, R.; Steinberg, S. Bonding diversity in rock salt-type tellurides: Examining the interdependence between chemical bonding and materials properties. *RSC Adv.* **2021**, *11*, 20679–20686. [CrossRef]
25. Hempelmann, J.; Müller, P.C.; Konze, P.M.; Stoffel, R.P.; Steinberg, S.; Dronskowski, R. Longe-Range Forces in Rock-Salt-Type Tellurides and How they Mirror the Underlying Chemical Bonding. *Adv. Mater.* **2021**, *33*, 2100163. [CrossRef]
26. Gladisch, F.C.; Steinberg, S. Revealing the Nature of Bonding in Rare-Earth Transition-Metal Tellurides by Means of Methods Based on First Principles. *Eur. J. Inorg. Chem.* **2017**, *2017*, 3395–3400. [CrossRef]
27. Göbgen, K.C.; Gladisch, F.C.; Steinberg, S. The Mineral Stützite: A Zintl-Phase or Polar Intermetallic? A Case Study Using Experimental and Quantum-Chemical Techniques. *Inorg. Chem.* **2018**, *57*, 412–421. [CrossRef]
28. Göbgen, K.C.; Fries, K.S.; Gladisch, F.C.; Dronskowski, R.; Steinberg, S. Revealing the Nature of Chemical Bonding in an $ALn_2Ag_3Te_5$-Type Alkaline-Metal (A) Lanthanide (Ln) Silver Telluride. *Inorganics* **2019**, *7*, 70. [CrossRef]
29. Eickmeier, K.; Fries, K.S.; Gladisch, F.C.; Dronskowski, R.; Steinberg, S. Revisiting the Zintl-Klemm Concept for $ALn_2Ag_3Te_5$-Type Alkaline-Metal (A) Lanthanide (Ln) Silver Tellurides. *Crystals* **2020**, *10*, 184. [CrossRef]
30. Eickmeier, K.; Steinberg, S. Revealing the Bonding Nature in an $ALnZnTe_3$-Type Alkaline-Metal (A) Lanthanide (Ln) Zinc Telluride by Means of Experimental and Quantum-Chemical Techniques. *Crystals* **2020**, *10*, 916. [CrossRef]
31. Smid, S.; Steinberg, S. Probing the Validity of the Zintl-Klemm Concept for Alkaline-Metal Copper Tellurides by Means of Quantum-Chemical Techniques. *Materials* **2020**, *13*, 2178. [CrossRef]
32. Eickmeier, K.; Steinberg, S. Exploring the frontier between polar intermetallics and Zintl phases for the examples of the prolific $ALnTnTe_3$-type alkali metal (A) lanthanide (Ln) late transition metal (Tn) tellurides. *Z. Naturforsch. B* **2021**, *76*, 635–642. [CrossRef]
33. Gladisch, F.C.; van Leusen, J.; Passia, M.T.; Kögerler, P.; Steinberg, S. $Rb_3Er_4Cu_5Te_{10}$: Exploring the Frontier between Polar Intermetallics and Zintl-Phases via Experimental and Quantumchemical Approaches. *Eur. J. Inorg. Chem.* **2021**, *2021*, 4946–4953. [CrossRef]
34. Gladisch, F.C.; Pippinger, T.; Meyer, J.; Pries, J.; Richter, J.; Steinberg, S. Examination of a Structural Preference in Quaternary Alkali-Metal (A) Rare-Earth (R) Copper Tellurides by Combining Experimental and Quantum-chemical Means. *Inorg. Chem.* **2022**, *61*, 9269–9282. [CrossRef] [PubMed]
35. Eickmeier, K.; Poschkamp, R.; Dronskowski, R.; Steinberg, S. Exploring the Impact of Lone Pairs on the Structural Features of Alkaline-Earth (A) Transition-Metal (M,M') Chalcogenides (Q) $AMM'Q_3$. *Eur. J. Inorg. Chem.* **2022**, *2022*, e202200360. [CrossRef]
36. Koch, P.; Steinberg, S. Exploring the subtle factors that control the structural preferences in Cu_7Te_4. *J. Phys. Condens. Matter* **2023**, *35*, 064003. [CrossRef] [PubMed]

37. Simons, J.; Steinberg, S. Identifying the Origins of Vacancies in the Crystal Structures of Rock Salt-type Chalcogenide Superconductors. *ACS Omega* **2019**, *4*, 15721–15728. [CrossRef]
38. Hulliger, F.; Hull, G.W. Superconductivity in rocksalt-type compounds. *Solid State Sci.* **1970**, *8*, 1379–1382. [CrossRef]
39. Moodenbaugh, A.R.; Johnston, D.C.; Viswanathan, R.; Shelton, R.N.; DeLong, L.E.; Fertig, W.A. Superconductivity of Transition Metal Sulfides, Selenides, and Phosphides with the NaCI Structure. *J. Low Temp. Phys.* **1978**, *33*, 175–203. [CrossRef]
40. Zaanen, J.; Chakravarty, S.; Senthil, T.; Anderson, P.; Lee, P.; Schmalian, J.; Imada, M.; Pines, D.; Randeria, M.; Varma, C.; et al. Towards a complete theory of high T_c. *Nat. Phys.* **2006**, *2*, 138–143. [CrossRef]
41. Bardeen, J.; Cooper, L.N.; Schrieffer, J.R. Theory of Superconductivity. *Phys. Rev.* **1957**, *108*, 1175–1204. [CrossRef]
42. Gabovich, A.M.; Voitenko, A.I.; Ausloss, M. Charge- and spin-density waves in existing superconductors: Competition between Cooper pairing and Peierls or excitonic instabilities. *Phys. Rep.* **2002**, *367*, 583–709. [CrossRef]
43. Simon, A. Superconductivity and Chemistry. *Angew. Chem. Int Ed. Engl.* **1997**, *36*, 1788–1806. [CrossRef]
44. Simon, A. Superconductivity—A source of surprises. *Solid State Sci.* **2005**, *7*, 1451–1455. [CrossRef]
45. Vaitheeswaran, G.; Kanchana, V.; Svane, A.; Christensen, N.E.; Olsen, J.S.; Jorgensen, J.-E.; Gerward, L. High-pressure stuctural study of yttrium monochalcogenides from experiment and theory. *Phys. Rev. B Condens. Matter Mater. Phys.* **2011**, *83*, 184108. [CrossRef]
46. Flahaut, J.; Domange, L.; Guittard, M.; Pardo, M.-P.; Partie, M. Nouveaux résultats relatifs à l'etude cristallographique des sulfures, séléniures et tellurures $L_{2\times3}$ des éléments des terres rares, de l'yttrium et du scandium. *CR Hebd. Séances Acad. Sci.* **1963**, *257*, 1530–1533.
47. Dronskowski, R. *Computational Chemistry of Solid State Materials*; WILEY-VCH: Weinheim, Germany, 2005.
48. Hoffmann, R. How Chemistry and Physics Meet in the Solid State. *Angew. Chem. Int. Ed.* **1987**, *26*, 846–878. [CrossRef]
49. Rustige, C.; Brühmann, M.; Steinberg, S.; Meyer, E.; Daub, K.; Zimmermann, S.; Wolberg, M.; Mudring, A.-V.; Meyer, G. The Prolific $\{ZR_6\}X_{12}R$ and $\{ZR_6\}X_{10}$ Structure Types with Isolated Endohedrally Stabilized (*Z*) Rare-Earth Metal (*R*) Cluster Halide (*X*) Complexes. *Z. Anorg. Allg. Chem.* **2012**, *638*, 1922–1931. [CrossRef]
50. Steinberg, S.; Brgoch, J.; Miller, G.J.; Meyer, G. Identifying a Structural Preference in Reduced Rare-Earth Metal Halides by Combining Experimental and Computational Techniques. *Inorg. Chem.* **2012**, *51*, 11356–11364. [CrossRef]
51. Steinberg, S.; Bell, T.; Meyer, G. Electron Counting Rules and Electronic Structure in Tetrameric Transition-Metal (T)-Centered Rare-Earth (R) Cluster Complex Halides (X). *Inorg. Chem.* **2015**, *54*, 1026–1037. [CrossRef]
52. Deringer, V.L.; Lumeij, M.-W.; Stoffel, R.P.; Dronskowski, R. Mechanisms of Atomic Motion Through Crystalline GeTe. *Chem. Mater.* **2013**, *25*, 2220–2226. [CrossRef]
53. Pyykkö, P. Strong Closed-Shell Interactions in Inorganic Chemistry. *Chem. Rev.* **1997**, *97*, 597–636. [CrossRef] [PubMed]
54. Gladisch, F.C.; Steinberg, S. Revealing Tendencies in the Electronic Structures of Polar Intermetallic Compounds. *Crystals* **2018**, *8*, 80. [CrossRef]
55. Steinberg, S.; Dronskowski, R. The Crystal Orbital Hamilton Population (COHP) Method as a Tool to Visualize and Analyze Chemical Bonding in Intermetallic Compounds. *Crystals* **2018**, *8*, 225. [CrossRef]
56. Burdett, J.K.; Hughbanks, T. Niobium oxide (NbO) and titanium oxide (TiO): A study of the structural and electronic stability of structures derived from rock salt. *J. Am. Chem. Soc.* **1984**, *106*, 3101–3113. [CrossRef]
57. Burdett, J.K.; Mitchell, J.F. Electronic Origin of Nonstoichiometry in Early-Transition-Metal Chalcogenides. *Chem. Mater.* **1993**, *5*, 1465–1473. [CrossRef]
58. Gladisch, F.C.; Maier, S.; Steinberg, S. Eu_2CuSe_3 Revisited by Means of Experimental and Quantum-Chemical Techniques. *Eur. J. Inorg. Chem.* **2021**, *2021*, 1510–1517. [CrossRef]
59. Blöchl, P.E. Projector augmented wave-method. *Phys. Rev. B Condens. Matter Mater. Phys.* **1994**, *50*, 17953–17979. [CrossRef] [PubMed]
60. Kresse, G.; Marsman, M.; Furthmüller, J. *Vienna Ab Initio Simulation Package (VASP), The User Guide*; Department of Computational Materials Physics, Faculty of Physics, University of Vienna: Vienna, Austria, 2010.
61. Kresse, G.; Furthmüller, J. Efficiency of ab-initio total energy calculations for metals and semiconductors using a plane-wave basis set. *J. Comput. Mater. Sci.* **1996**, *6*, 15–50. [CrossRef]
62. Kresse, G.; Furthmüller, J. Efficient iterative schemes for ab initio total-energy calculations using a plane-wave basis set. *Phys. Rev. B Condens. Matter Mater. Phys.* **1996**, *54*, 11169–11186. [CrossRef]
63. Kresse, G.; Hafner, J. Ab initio molecular dynamics for liquid metals. *Phys. Rev. B Condens. Matter Mater. Phys.* **1993**, *47*, 558–561. [CrossRef]
64. Kresse, G.; Joubert, D. From ultrasoft pseudopotentials to the projector augmented-wave method. *Phys. Rev. B Condens. Matter Mater. Phys.* **1999**, *59*, 1758–1775. [CrossRef]
65. von Appen, J. Quantenchemische Untersuchungen an Nitriden der Platingruppenmetalle. PhD Thesis, RWTH Aachen University, Aachen, Germany, 2006.
66. Stoffel, R.P.; Wessel, C.; Lumey, M. Ab Initio Thermochemistry of Solid-State Materials. *Angew. Chem. Int. Ed.* **2010**, *49*, 5242–5266. [CrossRef]
67. Perdew, J.P.; Burke, K.; Ernzerhof, M. Generalized Gradient Approximation Made Simple. *Phys. Rev. Lett.* **1996**, *77*, 3865–3868. [CrossRef]

68. Curtarolo, S.; Setyawan, W.; Hart, G.L.; Jahnatek, M.; Chepulskii, R.V.; Taylor, R.H.; Wang, S.; Xue, J.; Yang, K.; Levy, O.; et al. AFLOW: An automatic framework for high-throughput materials discovery. *Comput. Mater. Sci.* **2012**, *58*, 218–226. [CrossRef]
69. Ong, S.P.; Richards, W.D.; Jain, A.; Hautier, G.; Kocher, M.; Cholia, S.; Gunter, D.; Chevrier, V.L.; Persson, K.; Ceder, G. Python Materials Genomics (pymatgen): A Robust, Open-Source Python Library for Materials Analysis. *Comput. Mater. Sci.* **2013**, *68*, 314–319. [CrossRef]
70. Silvi, B.; Savin, A. Classification of chemical bonds based on topological analysis of electron localization functions. *Nature* **1994**, *371*, 683–686. [CrossRef]
71. Savin, A.; Nesper, R.; Wengert, S.; Fässler, T.F. ELF: The Electron Localization Function. *Angew. Chem. Int Ed. Engl.* **1997**, *36*, 1808–1832. [CrossRef]
72. Momma, K.; Izumi, F. VESTA 3 for three-dimensional visualization of crystal, volumetric and morphology data. *J. Appl. Crystallogr.* **2011**, *44*, 1272–1276. [CrossRef]
73. Maintz, S.; Deringer, V.L.; Tchougréeff, A.L.; Dronskowski, R. LOBSTER: A Tool to Extract Chemical Bonding from Plane-Wave Based DFT. *J. Comput. Chem.* **2016**, *37*, 1030–1035. [CrossRef]
74. Maintz, S.; Deringer, V.L.; Tchougréeff, A.L.; Dronskowski, R. Analytic Projection from Plane-Wave and PAW Wavefunctions and Application to Chemical-Bonding Analysis in Solids. *J. Comput. Chem.* **2013**, *34*, 2557–2567. [CrossRef]
75. Deringer, V.L.; Tchougréeff, A.L.; Dronskowski, R. Crystal Orbital Hamilton Population (COHP) Analysis as Projected from Plane-Wave Basis Sets. *J. Phys. Chem. A* **2011**, *115*, 5461–5466. [CrossRef] [PubMed]
76. Dronskowski, R.; Blöchl, P.E. Crystal Orbital Hamilton Populations (COHP). Energy-Resolved Visualization of Chemical Bonding in Solids Based on Density-Functional Calculations. *J. Phys. Chem.* **1993**, *97*, 8617–8624. [CrossRef]
77. Eck, B. *wxDragon 2.2.3*; RWTH Aachen University: Aachen, Germany, 2020.
78. Huppertz, H.; Heymann, G.; Schwarz, U.; Schwarz, M.R. High-Pressure Methods in Solid-State Chemistry. In *Handbook of Solid State Chemistry*; Dronskowski, R., Kikkawa, S., Stein, A., Eds.; Wiley-VCH: Weinheim, Germany, 2017.
79. Schwarz, K.; Blaha, P. DFT Calculations for Real Solids. In *Handbook of Solid State Chemistry*; Dronskowski, R., Kikkawa, S., Stein, A., Eds.; Wiley-VCH: Weinheim, Germany, 2017.
80. Hafner, J. Ab-Initio Simulations of Materials Using VASP: Density-Functional Theory and Beyond. *J. Comput. Chem.* **2008**, *29*, 2044–2078. [CrossRef] [PubMed]